OEA | Opto-Electronic Advances

Article

May 2026, Vol. 9, No. 5

Open Access

Highly sensitive SWCNT-based pyroelectric phototransistors for broadband room temperature infrared detection

Svetlana I. Serebrennikova[1], Daria S. Kopylova[1], Yuriy G. Gladush[1], Sakellaris Mailis[1], Nikita E. Gordeev[1], Aliya R. Vildanova[1], Aleksandr V. Averchenko[1], Sergey S. Zhukov[2], Dmitry V. Krasnikov[1] and Albert G. Nasibulin[1]*

Abstract: Thermal infrared (IR) detectors represent a crucial technology for various applications, yet achieving high performance without cooling remains challenging. Here, we demonstrate high-performance broadband IR photodetectors by integrating single-walled carbon nanotubes (SWCNTs) with a ferroelectric substrate, leveraging the pyroelectric effect for enhanced photodetection. Using aerosol chemical vapor deposition and capillary transfer techniques, we fabricate sparse SWCNT films on z-cut $LiNbO_3$ surfaces to create pyroelectrically gated field-effect transistors. The devices exhibit remarkable responsivity across the IR spectrum, with semiconducting channels achieving maximum relative responsivities reaching nearly 100 %/μW at 1550 nm. Our optimized SWCNT networks demonstrate exceptional specific detectivities of 1.7×10^{10} cm$\sqrt{\text{Hz}}$/W at 1550 nm and 1.4×10^{10} cm$\sqrt{\text{Hz}}$/W at 9.3 μm, surpassing graphene-based alternatives by several orders of magnitude and approaching theoretical limits. These results establish SWCNT-based pyroelectric photodetectors as promising candidates for room-temperature IR detection, eliminating the conventional requirement for cooling.

Keywords: photogating; carbon nanotubes; field effect transistor; photodetector; $LiNbO_3$

DOI: 10.29026/oea.2026.260019 | CSTR: 32247.14.oea.2026.260019

Citation: Serebrennikova SI, Kopylova DS, Gladush YG et al. Highly sensitive SWCNT-based pyroelectric phototransistors for broadband room temperature infrared detection. *Opto-Electron Adv* **9**, 260019 (2026).

1 Introduction

Thermal photodetectors that operate without cooling requirements are highly desirable devices for thermal imaging, quality control, and optical communication applications[1,2]. These photodetectors primarily utilize the pyroelectric effect, which occurs when absorbed radiation causes temperature modulation and subsequent change in spontaneous electric polarization[3]. In the detection process, the pyroelectric component functions as a capacitor, where the pyroelectric effect alters its electrostatic charge. Consequently, the photocurrent generated is directly proportional to the rate of the temperature change.

Recent research has introduced an innovative application where thermally driven electrical polarization changes in a pyroelectric crystal act as a back gate for a conductive channel deposited on the crystal polar surfaces (photogating effect), creating pyroelectrically gated field-effect transistors (FETs)[4–14]. Unlike traditional pyroelectric detectors, these devices can process continuous and pulsed light signals. The most extensively researched configuration uses graphene channels on $LiNbO_3$ polar faces[6–8,12], taking advantage of the pyroelectric effect caused polarization changes along the crystal *z*-axis[15–17]. This allowed the creation of pyroelectrically gated phototransistors[6–8], where depending on the polar face of the crystal one could produce either positive or negative gate voltage in contact with the channel material. Moreover, p-n junctions can be produced in channels formed on *x*-cut or on ferroelectric domain-engineered substrates[11–13]. However, the phototransistors based on graphene channels on *z*-cut $LiNbO_3$ exhibited low specific detectivity of $D^* = 1.14 \times 10^5$ cm$\sqrt{\text{Hz}}$/W (tested at a wavelength of $\lambda = 9$ μm[6]) compared to conventional pyroelectric detectors ($D^* = 8 \times 10^8$ cm$\sqrt{\text{Hz}}$/W for TriGlycine Sulphate

Received: 21 January 2026

Accepted: 27 March 2026

Published online: 7 May 2026

[1]Skolkovo Institute of Science and Technology, Nobel 3, Moscow 121205, Russia; [2]Moscow Institute of Physics and Technology, (National Research University), Institutskiy Per 9, Dolgoprudny, Moscow Region 141701, Russia.
*Correspondence: AG Nasibulin, E-mail: a.nasibulin@skoletch.ru

(TGS) pyrodetector[1]). This low detectivity stems from the lack of a band gap in graphene, which restricts conductivity modulation with the gate voltage[18]. To enhance the device's performance, we suggest replacing the graphene channel with single-walled carbon nanotubes (SWCNTs).

SWCNTs present a compelling platform for next-generation photodetector applications due to their unique electronic properties[19–27]. Notably, semiconducting SWCNTs (s-SWCNTs), comprising approximately two-thirds of as-grown nanotubes, exhibit gate-voltage sensitivity owing to their intrinsic bandgap[19]. While conventional approaches typically employ individual SWCNTs[19,28] or purified s-SWCNT films[29,30] as FET channels, our previous research has demonstrated the efficacy of sparse SWCNT networks in enhancing photogating-based FET performance on Si/SiO_2 substrates showing that strategic deployment of SWCNT networks near the percolation threshold effectively mitigates the impact of metallic nanotubes (m-SWCNTs) in the as-synthesized networks[31]. However, achieving consistent device performance with randomly oriented SWCNT networks remains challenging[28–32]. The solution lies in synthesizing and transferring homogeneous, defect-free networks of long SWCNTs – a crucial requirement for maintaining high carrier mobility.

Here, we present an innovative approach utilizing percolation sparse networks of high-quality SWCNTs as FET channels on $LiNbO_3$, leveraging the pyroelectric effect for achieving a photoresponse. Modifying the conventional aerosol CVD synthesis technique, we can produce thin SWCNT films ranging from sub-monolayer to hundreds of nanometers to enhance photodetector performance, particularly the signal-to-noise ratio, compared to graphene-channel alternatives. The implementation of pyroelectric gating extends the operational spectrum into the mid-infrared (MIR) region, surpassing the limitations of Si/SiO_2-based photogating FETs, which are constrained by silicon IR absorption range. Our comprehensive investigation examines the relationship between channel parameters and photoresponse characteristics, including amplitude and temporal dynamics across various wavelengths. This research establishes the foundation for a novel class of room-temperature broadband photodetectors with enhanced sensitivity.

2 Methods and materials

2.1 Characterisation of SWCNTs and $LiNbO_3$

Raman spectra were analyzed using a LabRAM HR Evolution system with 532 nm 1 mW laser excitation. SEM images were collected with Quattro S, Thermo Fisher Scientific. AFM visualisation was performed with Bruker Multimode V8. TEM images were collected with Tecnai G2 F20 microscope. The absorbance and transmission spectra were obtained with PerkinElmer Lambda 1050 UV–vis–NIR spectrometer (250–2500 nm) and Bruker Vertex 70v FTIR spectrometer (2500–25000 nm).

2.2 SWCNTs transferring

At the first step, a filter (Merck Millipore HAWP filter membranes with 0.45 μm pore chosen for low adhesion to CNTs) with SWCNTs is annealed at 130 °C for 15 minutes to improve the adhesion of the nanotubes to the substrate. Secondly, a piece of filter which has to be 0.5–1 mm larger in length and width than the substrate to cover it fully is cut and placed on the substrate (the filter's side with film must lie on the substrate surface) as shown in Fig. 1(a). Next, the isopropanol (IPA, 99.8%, ∼ 100 μL) is sprayed to wet the whole substrate and the filter and present the surface tension, and then they are put under a pressure of 2–5 MPa for 30 seconds. When the filter is completely dry, it can be removed. The success of SWCNT network transfer is controlled with 2-probe resistance measurement of the filter (which shows 10–40 MΩ before transfer and achieves the limit of detection of multimeter after transfer) and with Raman spectroscopy by the intensity of G-peak.

2.3 Fabrication of FETs

We used UV lithography to pattern contacts (μPG101 Heidelberg instruments Micro Pattern Generator) on the device that consisted of an adhesion layer of chromium (5 nm) and gold (60 nm) deposited by thermal evaporation (Tecuum AG vacuum evaporator) with subsequent lift-off process (Fig. 1(a)). The channel length of individual devices varied from 10 to 310 μm, and the width of the channels was fixed at the value of 150 μm. A second lithographic step was used in conjunction with oxygen plasma to microstructure the continuous SWCNT film for the purpose of electrically isolating individual devices. 10% of the devices underwent wire bonding with F&S Bondtec bonder to facilitate the measurement of the response to 9.3 μm illumination due to the optical setup. The control FETs on Si/SiO_2 substrate (n-doped silicon with dopants concentration $\sim 10^{15}$ cm^{-3}, SiO_2 layer thickness is ~ 1 μm) were fabricated with the same procedure.

2.4 Photoresponse measurement

We measured the electrical characteristics and photoresponse of the devices using a Keysight B15000A semiconducting device analyser and/or Keithley 2636B source meter connected to a TS150 probe station. The measurements of the photoresponse were conducted using a source-drain voltage of $V_{sd} = 1$ V. A 532 nm green diode laser (1–100 mW per 5 mm^2), a 1550 nm infrared diode laser (0.5–15 mW per 10 mm^2) and a 9.3 μm quantum cascade laser (2.5–16.5 mW per 15 mm^2) were used as light stimuli to

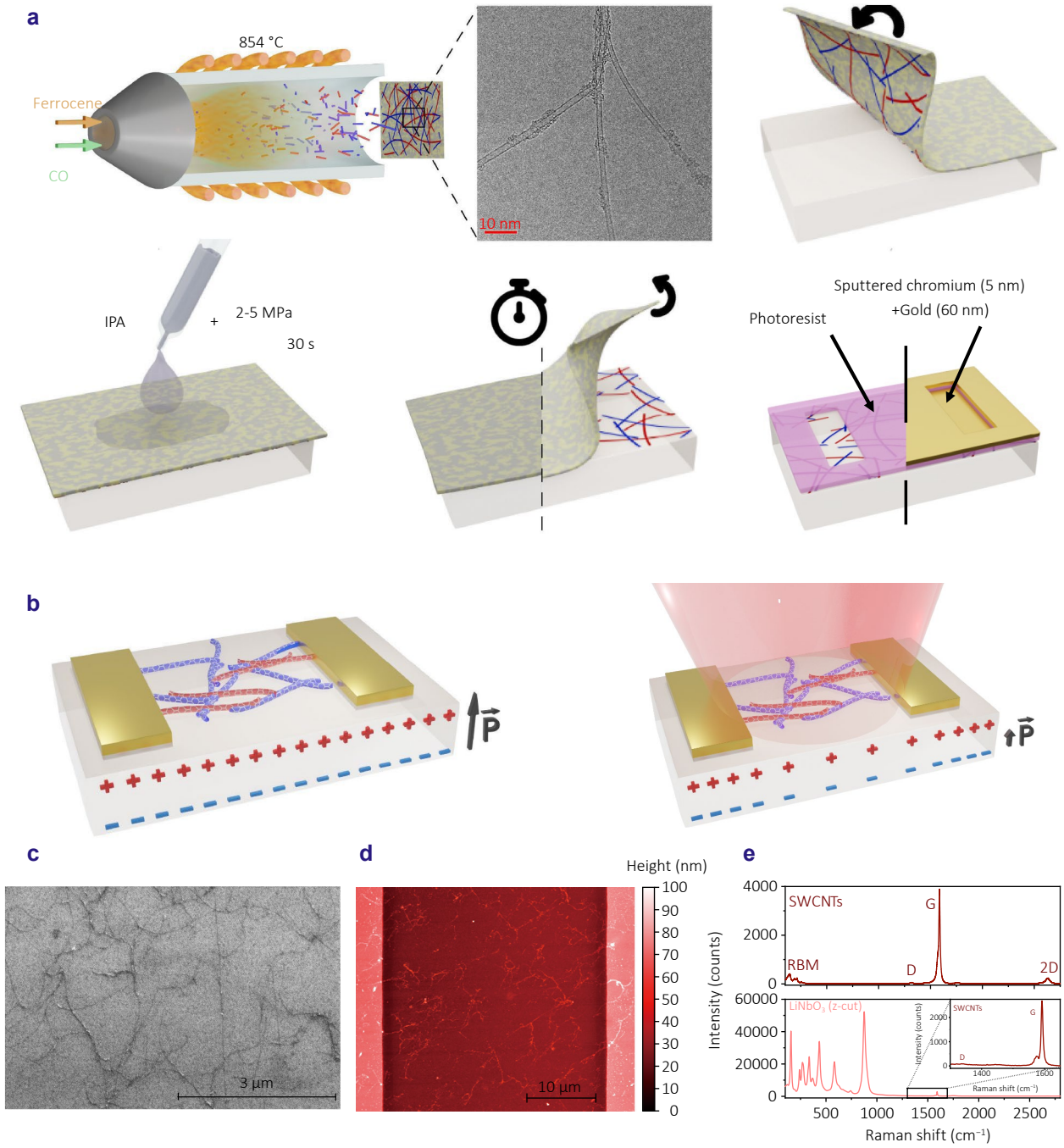

Fig. 1 | Device preparation and characterization. (a) Schematic presentation of the synthesis of SWCNTs by the aerosol CVD method, collection of the sparse network on a nitrocellulose filter, and subsequent capillary transferring on a substrate and contact patterning and deposition. (b) Schematics of the fabricated pyroelectric $LiNbO_3$ phototransistors (SWCNTs are transferred onto "+z face" of the crystal; blue tubes corresponds to s-SWCNTs, red ones are m-SWCNTs) and mechanism of channel gating with radiation. (c) SEM image of the sparse SWCNT network on Si/SiO_2 substrate. (d) AFM image of the sparse SWCNT network between two gold contacts on a Si/SiO_2 substrate. (e) Raman spectra of thick film of SWCNTs used for the phototransistor fabrication (upper spectrum) and SWCNTs on the z-cut $LiNbO_3$ substrate (lower spectrum).

observe photogating. The illuminating power level was controlled by regulating the current directly from the power supply of each laser. We utilised a Peltier heater to conduct measurements at different temperatures. Finally, we used a Zurich MFLI Lock-In amplifier to obtain the transistors' noise spectral density $I_n/\sqrt{\Delta f} = 0.1 - 100$ $\mathrm{pA}/\sqrt{\mathrm{Hz}}$ in $\Delta f = 1$ Hz bandwidth within the frequency range of 0.1–100 Hz, which shows ~$1/f$ behaviour (Fig. S9). The simulation of the $LiNbO_3$ substrate heating was performed with COMSOL Multiphysics 6.1.

3 Results and discussion

3.1 Device preparation and characterisation

The exceptional properties of SWCNTs, including their high carrier mobility and tunable bandgaps, position them as an ideal candidate for advanced photodetection applications and bolometric devices, with performance metrics rivalling traditional vanadium oxide-based systems[33–36]. Conventional methods for thin film formation prove to be inadequate for producing sparse percolation networks of long, defect-free SWCNTs. Traditional ultrasonication followed by ultracentrifugation or filtration processes results in nanotube fragmentation and irreversible surfactant adhesion. To overcome these limitations, we developed a modified aerosol chemical vapor deposition (CVD) approach – an advanced synthesis technique utilizing floating catalyst reactors with extreme catalyst dilution[27]. This method enables the formation of individual nanotubes or minimal bundles through reduced collision probability in the aerosol phase.

Our modified aerosol CVD process employs carbon monoxide decomposition on Fe-based aerosol catalysts generated through ferrocene pyrolysis[37–39]. The methodology allows precise control over film density through synthesis and collection time optimization, with SWCNT films deposited on nitrocellulose filters. SWCNT films are first deposited on nitrocellulose filters, and the network density is pre screened by two probe resistance measurements directly on the filter. Filter resistances in the range of $10-40$ MΩ are selected as optimal, as they correspond to sub metallic percolation networks that nevertheless remain laterally continuous over several hundred micrometers, thus suppressing metallic percolation while maintaining overall connectivity[30–32]. Here, we addressed the traditional challenge of transferring ultrathin networks—typically considered non-transferable without filter dissolution and subsequent organic contamination—through an innovative capillary transfer technique[30–32]. This method enables direct network transfer from a filter to a substrate yielding uniform and high-quality sparse nanotube networks (Fig. 1(a)). Quantitative image analysis gives a typical areal density of 100±30 individual SWCNTs and small bundles (2–3 tubes, length ≈ 10 μm) per 100 μm^2, with an average inter bundle spacing of ∼1 μm, confirming that the networks are well within the sparse, sub percolating regime (Fig. 1(c, d)).

Structural and spectroscopic characterization confirms the exceptional quality of the synthesised SWCNT networks. Scanning electron and atomic force microscopy reveals the distinctive morphology of the sparse network architecture of ∼10 μm long SWCNTs on silicon substrates (Figs. 1(c, d) and S1), while Raman spectroscopy of films on $LiNbO_3$ substrates demonstrates characteristic peaks: the G-mode (≈ 1592 cm^{-1}, indicative of sp^2 carbons) and D-mode (≈ 1327 cm^{-1}, associated with carbon defects) (Fig. 1(e)). The remarkable G/D intensity ratio of 100±15 validates the exceptional structural integrity of the SWCNTs. For photodetector fabrication, we employed 500 μm-thick $LiNbO_3$ *z*-cut single-crystal substrates, with Raman characterization confirming the material quality (Fig. 1(e))[40]. The "congruent melting" $LiNbO_3$ crystal composition exhibit high Curie temperature (≈1210 °C) and large coercive fields which results in a polarization domain stability at low temperatures. Thus, in the experiments presented in this work the fluctuations charged defect cites, which leads to the full polarization inversion and fatigue, is negligible[15].

3.2 Investigation of the photoresponse mechanism

Sparse networks of randomly oriented SWCNTs consisting of a mixture of s-SWCNTs and m-SWCNTs used as the FET's channel demonstrates variations in the measured conductivity from channel to channel as it depends on the nanotube density and the local fraction of metallic species. The conductivity variation, therefore, leads to the variation in the response of each channel to the gating[30,31,41,42]. The channels can be divided into "metallic", when m-SWCNTs percolate from the source to the drain contacts, or "semiconducting" otherwise (Fig. 1(b)). Generally, the probability of a "metallic" channel occurrence is higher for 1) denser SWCNT network, 2) wider contacts, and 3) shorter channel lengths[41]. In our previous work, the channel conductivity type ("metallic" or "semiconducting") on Si/SiO_2 substrates was identified by the I_{on}/I_{off} ratio of the transistor–the current ratio of fully opened and fully closed channels, controlled by the gate voltage V_g, as can be seen on the typical transfer characteristics (dependence of the channel current I_{sd} on V_g, Fig. S2(a))[31]. On a given substrate containing an array of ∼100 transistors, the typical fraction of semiconducting devices ($I_{on}/I_{off} > 100$) exceeds 60%, and increases to about 80%–90% for channel lengths > 30 μm, which are notably larger than the average SWCNT bundle size (Fig. S2(b)). This behaviour reflects the reduced probability of purely metallic percolation paths in longer channels[30,31].

In the case of $LiNbO_3$-based phototransistors, the nature of the device channels cannot be identified by applying the backgate. In this situation, we use the distribution of channels' resistances normalised to their length R_{dark}, to characterise channel metallicity. According to these values from control devices on Si/SiO_2 substrate, the resistances higher than 0.03 MΩ/μm correspond only to "semiconducting" devices with high $I_{on}/I_{off} >> 100$, while smaller resistance can be attributed to both "metallic" ($I_{on}/I_{off} < 100$) or "semiconducting" channel type (Fig. S2(b)). The same nominal boundary can be drawn at the resistance distribution of the studied devices on $LiNbO_3$ (Fig. S2(d)). In addition, the difference between "semiconducting" and "metallic" devices is traced in diode-like and linear *IV* characteristics correspondingly (Fig. S2(d), inset).

Due to the environmental doping at ambient conditions SWCNTs exhibit p-type conductivity[30,31,41,42], so the channels are opened at negative back-gate voltages and closed at positive ones (Fig. S2(a)). The channel response of the phototransistor depends on the face of the $LiNbO_3$ substrate, which is relevant to the orientation of the polarization (Fig. 2). For the "+z face", SWCNT channel lays on the side with positive surface charges, and for the "-z face", SWCNTs are on the negative charged surface. Moreover, since the charge density depends on temperature, we can mimic the channel resistance dependence on the gate voltage by varying the substrate temperature (Fig. 2). As $LiNbO_3$ has a negative pyroelectric coefficient of $p = -4 \times 10^{-5}$ $C/(Km^2)$, the heating of the crystal (using a Peltier element or by laser irradiation) leads to a reduction of the positive charge on the "+z face" in contact with the SWCNTs, which results in a decrease of the SWCNT channel resistance (Fig. 2(a, b)). The reverse process occurs for the SWCNT channel deposited on the "-z face", as shown in Fig. 2(c, d). The maximum values of the electric field arising due to the pyroelectric effect are $E = -p\Delta T/(\varepsilon_0\varepsilon) = \pm 1.6 \times 10^7$ V/m at $\Delta T = \pm 10$ K (where ε_0 is a vacuum permittivity, and $\varepsilon = 29$ is a $LiNbO_3$ permittivity[15]) corresponding to values that are able to open or close SWCNT channel from typical FETs' transfer curves $E = \pm 10^8$ V/m for $V_g = \pm 10$ V and SiO_2 thickness ~ 1 μm (Fig. S2(a)). The range of the transistor's resistance change depends on the initial conductivity of the channel: more than four orders of magnitude for the "semiconducting" and less than two orders for the "metallic" channel with the maximum absolute values of the slope dR/dT achieving $\sim 10^{10}$ MΩ/μmK^{-1} and $\sim 10^6$ MΩ/μmK^{-1}, respectively (Fig. 2). This strong decrease of dR/dT with increasing film metallicity highlights that the highest response to the gate change is achieved in sparse networks with low metallic percolation.

The $R_{dark}(\Delta T)$ dependence (Fig. 2) and the transfer curve (Fig. S2(a)) exhibit reproducible hysteresis corresponding to an effective gate voltage window of approximately of 5–10 V, which is likely caused by pre-existing surface charges residing on the polar surfaces of $LiNbO_3$ and from charge trapping by environmental species (oxygen, water, nitrogen oxides) at the SWCNT/substrate interface as well as from slowly relaxing compensating charges responding to temperature induced changes in the bulk $LiNbO_3$ dipole moment[42–46]. Nevertheless, the devices maintain stable performance over at least $\sim$ 100 optical on/off cycles under 532 nm and 1550 nm illumination and $\sim$ 10 thermal cycles of ΔT±10 K (at heating rate of 2 – 5 K/s) around room

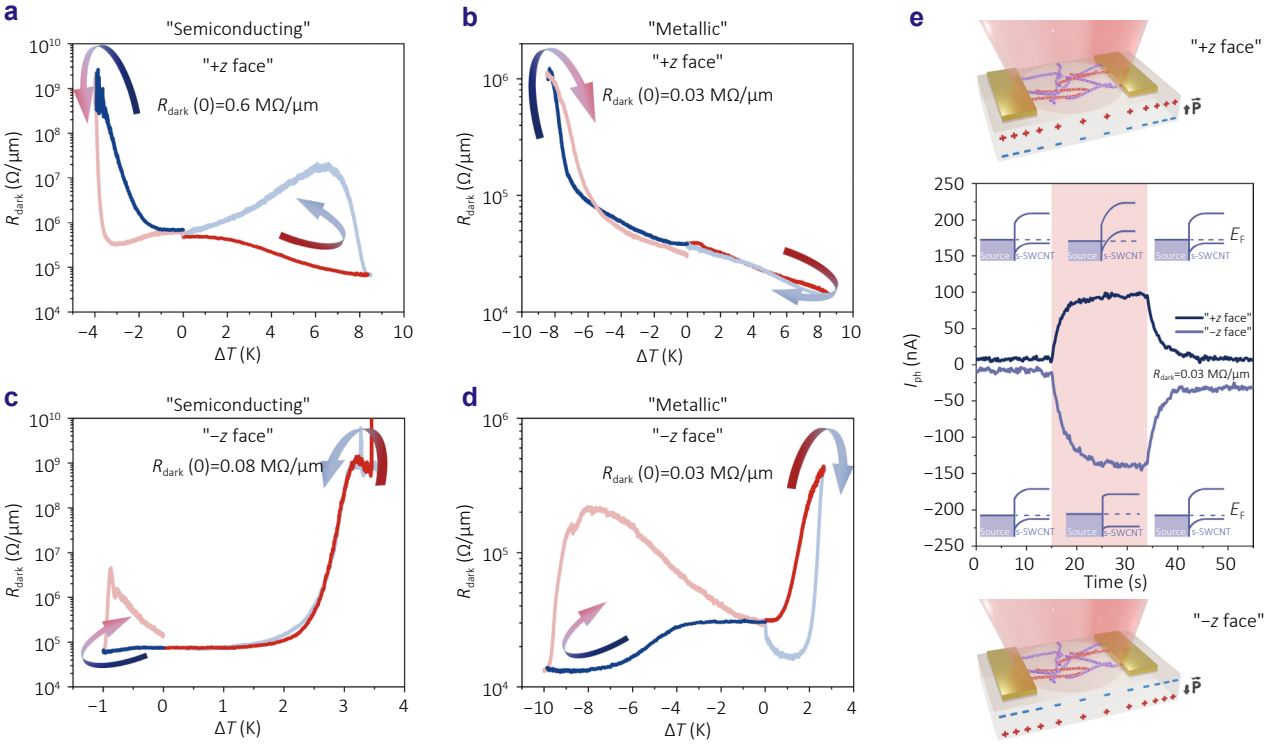

Fig. 2 | Dependence of the SWCNT channel resistance on small temperature changes around room temperature (RT = 24 °C) for: (a) "semiconducting" and (b) "metallic" transistors fabricated on the "+z face" of the substrate (dark blue/red lines represent cooling/heating with Peltier, light red/blue lines shows heating/cooling of the sample). (c) "semiconducting" and (d) "metallic" transistors fabricated on the "-z face" of the substrate. (e) Change in SWCNT channel's current in response to illumination with 1550 nm laser source (P = 5 μm per device area) for transistors fabricated on different faces of the $LiNbO_3$ substrates and schematics of the corresponding Fermi level E_F change of s-SWCNTs.

temperature (RT), without detectable degradation in pyroelectric response or transfer characteristics. It is worth noting, that in long time scales (>1 day) at a fixed temperature offset from RT, the compensation process in $LiNbO_3$ leads to a gradual return of the channel resistance resulting in a shift of the absolute starting point of the $R_{dark}(\Delta T)$ dependence (Fig. 2), while the slope and hysteresis width remain nearly unchanged. Therefore, ambient temperature variations in the 10–40 °C range primarily affect the baseline but do not impair the differential pyroelectric photogating response.

In addition, we measured the $R_{dark}(T)$ dependence of the sparse network on the reference Si/SiO_2 substrate within ±15 K around room temperature. The intrinsic bolometric response of the film is characterized by a linear slope of $dR/dT \approx -130\ \Omega/\mu mK^{-1}$ with always a negative sign with a consistently negative sign (Fig. S3(a)).

Furthermore, the photogating effect in transistors with SWCNT channel on $LiNbO_3$ was studied by illuminating the devices using several laser sources and measuring the photocurrent, which is defined as $I_{ph} = I_{light} - I_{dark}$ at different laser powers P, normalised to the area of the device (Fig. 3). Then, we calculated the absolute $S_I = I_{ph}/P$ and relative $S_{rel} = S_I/I_{dark} \times 100\%$ responsivities of the phototransistors. It should be stressed that $LiNbO_3$ has a wide transparency window from 350 to 5000 nm defined by the band gap (~ 3.5 eV) and phonon absorption at ≥ 5 μm (Fig. S4(a))[15–17]. We registered the increase in responsivity by a factor from 2 to ~ 8 at 1550 nm compared to 532 nm, probably because of the increased absorption of SWCNTs (Fig. S4(b)) independently on channels' R_{dark} (Figs. 3(a, d) and S5). And the slight rise of responsivity of the same detectors ($\sim 2-4$ times) between 1550 nm and 9.3 μm happens due to increased $LiNbO_3$ absorption in MIR region instead (Fig. 3(a, d)). Under identical 532 and 1550 nm illumination conditions, the reference devices on heavily doped Si/SiO_2 do not exhibit any detectable photoresponse. This confirms that the sign changing modulation of resistance observed in SWCNT/$LiNbO_3$ devices originates from the pyroelectric effect in substrate rather than from intrinsic photogating or bolometric effects in the SWCNT film.

The pyroelectric response of $LiNbO_3$ crystal produces a change in the surface charge, which is proportional to the modulation of the local temperature, which is, in turn, proportional to the incident radiation intensity[1–3]. The photogating voltage δV_{ph} produced with surface charge change is linked to the measured photocurrent in the following way: $I_{ph} = \delta V_{ph}(\partial I_{sd}/\partial V_g)$[47]. In Fig. 3(a, d), we can see a

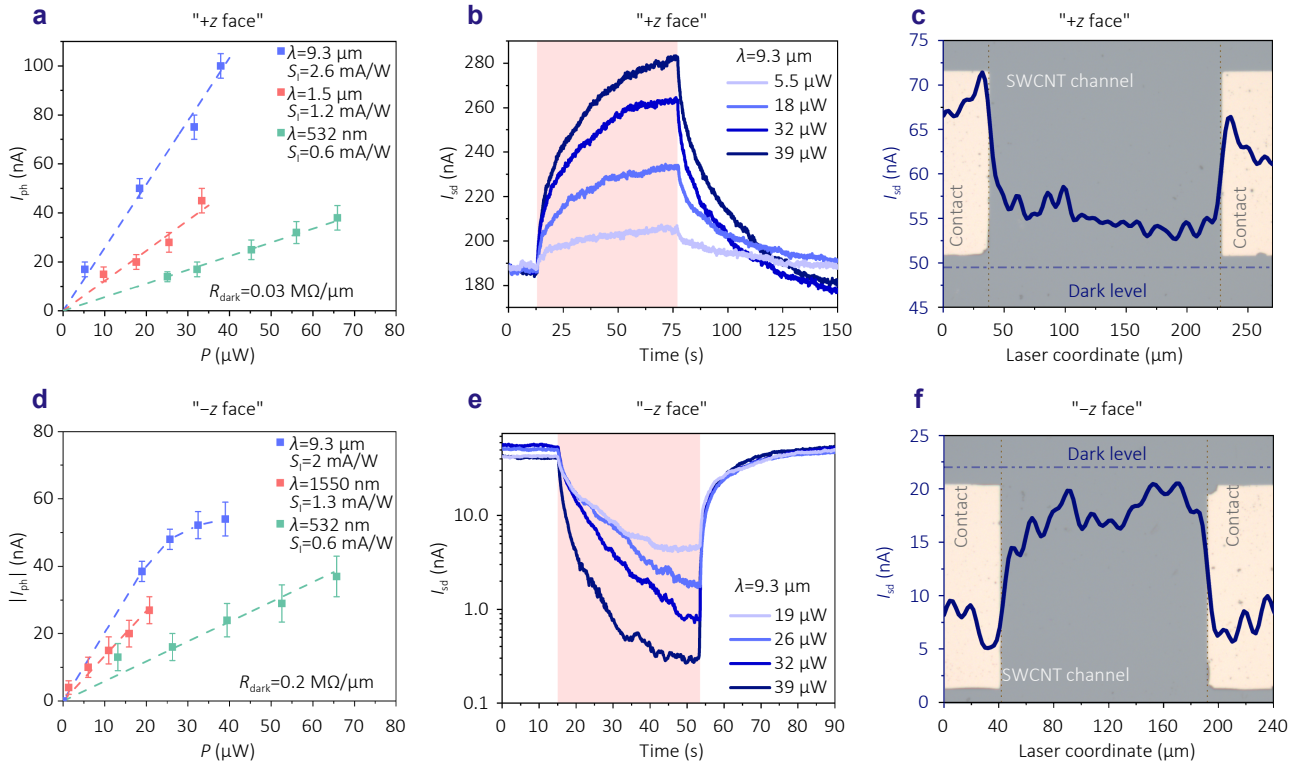

Fig. 3 | Photocurrent dependences on power and device position at different light wavelength for "+*z* and -*z* faces". (a, d) Photocurrent, corresponding to 532 nm (green dots), 1550 nm (red dots) and 9.3 μm (blue dots) illumination at different powers for the device on: (a) "+*z* face", (d) "-*z* face" of the $LiNbO_3$ substrate. (b, e) Time response of a phototransistor on (b) "+*z* face" and (e) "-*z* face" to 9.3 μm illumination. (c, f) Change of the SWCNT channel's current depending on the laser beam position (λ = 532 nm, P = 4 mW, D = 20 μm, scan velocity = 10 μm/s) superimposed on the optical microscope image of the corresponding channel of the phototransistor on: (c) "+*z* face"; (f) "-*z* face".

linear growth of the photocurrent with the laser power which at low values corresponds to the photogating voltage, that does not fully open or close the channel (with high absolute values of transfer curve's derivative at Fig. S2(c), from Fig. 2 the corresponding $\Delta T \leq \pm 1$ K). From the slope of the linear photocurrent dependence on the laser power we can determine the absolute responsivity. However, at the incident wavelength of 9.3 μm, we observed saturation of the photocurrent for devices fabricated on the "-*z* face", while at the same laser intensities for devices on the "+*z* face", the saturation of I_{ph} was not achieved (Figs. 3 and S6). This asymmetric response is attributed to the asymmetry and hysteresis in the transfer characteristics of the SWCNT FETs with respect to $V_g = 0$ V, which is also evident from the temperature dependence of the SWCNT FET resistance on $LiNbO_3$ shown in Fig. 2. Thus, it leads to the different optical power level required to obtain current saturation at I_{off} for "-*z* face" (corresponds to the lower branch of transfer curve and values of its derivative close to the 0 in Fig. S2(c)), and at I_{on} for "+*z* face" (corresponds to the upper branch of transfer curve and higher absolute values of its derivative Fig. S2(c)), and illumination at maximum powers of 9.3 μm corresponds to the heating $\Delta T = 3 - 4$ K. In contrast to the absolute responsivity, the relative responsivity can reach several orders of magnitude for transistors on the "-*z* face" with laser or external heating depending on the type of the channel (Fig. S6). The asymmetry of the SWCNT FET's transfer characteristics also results in the dissimilarity in relative responsivity measured to 1550 nm from devices on different faces of $LiNbO_3$ (Fig. S3(b)).

The observed strong absolute and relative responses of the SWCNTs phototransistors to the substrate's electric polarization change, induced by direct heating and by irradiation, resulted from high I_{on}/I_{off} ratios (up to $\sim 10^5$) and low I_{off} (~ 1 pA) achieved for the transistor with "semiconducting" channels (Figs. 2 and S2(a)) and attributed to the modulation of the Schottky barrier between SWCNTs and metal contacts with gate voltage[45,46]. To investigate the role of the contact between SWCNTs and metal in the process of photoresponse, we scanned the transistor's channel with a focused laser beam at the wavelength, where the $LiNbO_3$ absorption is low ($\lambda = 532$ nm, $P = 4$ mW, diameter $D = 20$ μm < channel length) with the velocity of 10 μm/s and recorded the current I_{sd} ($V_{sd} = 1$ V) (Fig. 3(c, f)). Thus, we observed a significant drop of the photocurrent when the beam crosses the channel due to low absorption and heat propagation in $LiNbO_3$ and a rise of I_{ph} when the beam meets the metal contact edge again (Fig. 3(c, f)).

3.3 Characteristics of the phototransistors

Even though the mechanisms of photogating in Si/SiO_2 and $LiNbO_3$ substrates are different, we observed similar trends of the photoresponse dependence on the channel's dark conductivity. As expected, the responsivity drops with the increase of the channel resistance R_{dark}, achieving a maximum absolute responsivity of $S_I = 80$ mA/W for less resistive devices (< 0.03 MΩ/μm), which are likely to be "metallic" and are associated with larger absolute values of photocurrent (Fig. 4(a)). On the other hand, the relative responsivity grows with the channel's resistance. Therefore, the highest relative responsivity S_{rel} of 98.8 %/μW corresponds to the more resistive ("semiconducting") device. In contrast, for the most conductive devices, the relative responsivity S_{rel} does not exceed 1 %/μW in (< 0.03 MΩ/μm) (Fig. 4(b)). The same trends of characteristics were observed for illumination with both 1550 nm and 9.3 μm radiation (Figs. 4(a, b) and S8). The maximum measured values of absolute and relative responsivities were 6 mA/W and 8 %/μW, respectively, for the devices that were illuminated with 9.3 μm, representing a significant performance improvement as compared to previously reported phototransistors (Table 1)[4–8].

Moreover, from the current dynamics with/without illumination (Fig. 2(e)), we determined the on- and off-response time when the change in current reaches the level of $(1 - 1/e)$ of the maximum value[1,2]. Since the intrinsic thermal conductivity of individual SWCNTs is of order 10^3 W/(m·K)[33], the response time of pyroelectric detectors is defined by the rate of heat propagation through the $LiNbO_3$ substrate[1–3]: $\tau = C_{th}/G_{th}$, where C_{th} is the specific heat capacity of 628 J/(kg·K), and G_{th} is the thermal conductivity of 5.2 W/(m·K) of $LiNbO_3$[17]. $LiNbO_3$ has a low thermal conductivity, which leads to a slow response. The photogating detectors reported here based on the pyroelectric effect have an average response time $\tau \sim 2$ s which corresponds with the previously reported results for devices on 500 μm thick substrates (Table 1)[6–8,12]. To estimate the main reason of this result we applied a COMSOL Heat Transfer in Solids package with deposited Gaussing beam of 9.3 μm, $D = 3$ mm and $P = 8$ mW as a heat source and emissivity of $LiNbO_3$ external surface ≈ 0.9 at this wavelength[17]. The bottom surface was studied for the heat flux between it and the stage where the sample is placed during the measurement. From the temperature dependence through time in the substrate surface center right under the incidence of the beam and comparing it with the slowest (Figs. 3(b, e), S6), we obtained that the effective thermal conductance between the sabstrate and the stage for described experiments is ≥ 150 W/(m^{2}K) (Fig. S7(a)). The slow compared to semiconductor photodiodes thermal time constant of the presented SWCNT/$LiNbO_3$ phototransistors is still comparable to many conventional pyroelectric and thermal IR detectors used in non-dispersive gas sensing, environmental monitoring, and Fourier-transform IR spectroscopy, where typical response times are in the sub second to a few second range[1–3]. The response time in the current design is limited by heat diffusion through the 500 μm thick $LiNbO_3$

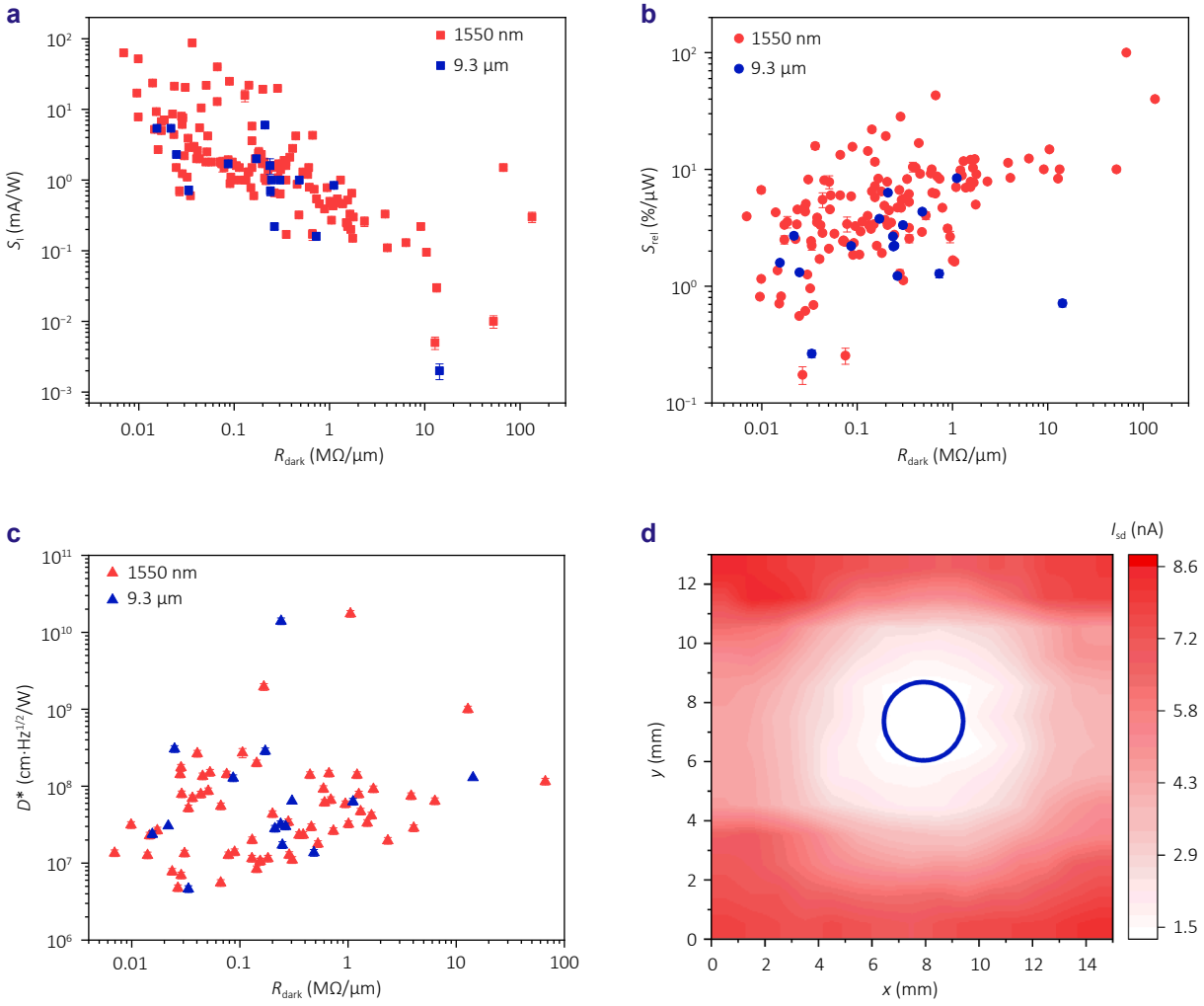

Fig. 4 | Characteristics of the phototransistors. (a) Absolute and (b) relative responsivities and (c) specific detectivity of SWCNT phototransistors with different resistances normalised to channels' lengths at 1550 nm and 9.3 μm laser. (d) Photocurrent distribution measured by scanning a phototransistor (SWCNTs on "-*z* face" $LiNbO_3$ substrate; V_{sd} = 0.2 V) with a quantum cascade laser operating at 9.3 μm with the laser power of 8 mW. A blue circle shows the real size of the beam (D = 3 mm).

substrate; therefore, faster variants could be realized in the future by employing thinner $LiNbO_3$ films or membrane structures and optimized thermal management (Fig. S7(b)).

The specific detectivity was calculated according to the following formula[1,2]: $D^* = S_I\sqrt{A\Delta f}/I_n$, where A is the area of the photodetector and $I_n/\sqrt{\Delta f}$ is the noise spectral density. As can be seen from Fig. 4(c), there is no noticeable dependence of the specific detectivity on the resistance since both responsivity (Fig. 4(a)) and noise (Fig. S9) are inversely proportional to the channel's resistance. The wide dispersion of D^* values can be explained by the wide range of responsivities that are registered at different channel resistances. Maximum values of detectivity were calculated to be $D^* = 1.7 \times 10^{10}$ cm$\sqrt{\text{Hz}}$/W (at 1550 nm) and $D^* = 1.4 \times 10^{10}$ cm$\sqrt{\text{Hz}}$/W (at 9.3 μm) corresponding to devices with a resistance of 0.3 MΩ/μm. These values are 5 orders of magnitude higher then the maximum specific detectivity of similar detectors fabricated with graphene channels reported by Gopalan et al. (Table 1)[6]. The combination of the thermal detector with the transistor geometry demonstrated in this work allowed us to achieve the detectivity values close to theoretical limit of $D^* = 1.98 \times 10^{10}$ cm$\sqrt{\text{Hz}}$/W for thermal detectors operated at room temperature[1].

To prove the applicability of our photodetector, we scanned two different size beams of a quantum cascade laser operating at $\lambda = 9.3$ μm with the device by moving the detector with the x-y translation stage with the scan rate of 1 mm/s (Fig. 4(d) where D of the incident beam is 3 mm, and Fig. S10 where $D = 15$ mm). Since the calculation of the heat distribution at the surface of $LiNbO_3$ substrate with the same dimensions lying on the perfect heat sink in response to the point source ($D = 0.2$ mm, $\lambda = 9.3$ μm) should

Table 1 | Comparison of characteristics of the photogating-based transistors with response caused by pyroelectric effect with channels of different low-dimensional materials.

Channel	Substrate	Mechanism	V_{sd} (V)	λ, (μm)	Maximum S_I (A/W)	Maximum S_{rel} (%/W)	Response time (s)	D^* (cm$\sqrt{\text{Hz}}$/W)	References
Graphene	PZT	FET	10	1.064	3.6×10^{-4}				Hsieh et al., 2012[4]
MoS_2	PMN-PT, 60 μm	FET-assist. photoresistor	0.5	1.064		500			Fang et al., 2015[5]
Graphene	$LiNbO_3$ *z*-cut, 500 μm	FET	0.1	6-10	1.5×10^{-4}		1.3	1.14×10^5	Gopalan et al., 2017[6]
Graphene	$LiNbO_3$ *z*-cut, 500 μm	FET	0.01	9	2.7×10^{-4}	2×10^4		6×10^4	Sassi et al., 2017[7]
Graphene	$LiNbO_3$ *z*-cut, 500 μm+SiN,100 nm	FET	0.1	7.9	7×10^{-4}		1		Shimatani et al., 2019[8]
Graphene	P(VDF-TrFE)	FET	2	0.66	7.9×10^{-4}				Wei et al., 2023[9]
MoS_2	$LiNbO_3$ *z*-cut, 600 nm	FET-assist. photoresistor	5	0.66	113.1		32×10^{-3}	7.2×10^{12}	Liu et al., 2025[10]
MoS_2	P(VDF-TrFE)	Bipolar transistor	0	0.532	12		32×10^{-6}	10^{13}	Lv et al., 2019[11]
Graphene	$LiNbO_3$ *x*-cut, 500 μm; 700 nm	p-n diode	2; 0.5	1.064	2.92×10^6; 1.78×10^5		23×10^{-3}; 3.3×10^{-3}	8.65×10^{14}; 3.32×10^{11}	Guan et al., 2021[12]
MoS_2	$LiNbO_3$ *x*-cut, 500 μm	p-n diode	2	0.462	17.3		0.25×10^{-3}	4.3×10^{11}	He et al., 2023[13]
SWCNTs	$LiNbO_3$ *z*-cut, 500 μm	FET	1	1.5; 9.3	8×10^{-2}; 6×10^{-3}	98×10^6; 8×10^6	2	1.7×10^{10}; 1.4×10^{10}	This study

result in a 0.51 mm hot spot on its surface (Fig. S10(b)), we attribute blurred and distorted beam image in comparison to its actual size (blue circle in Figs. 4(d) and S10(a)) to the imperfect heat sink (Fig. S7). This problem can be solved by covering the area outside of the detector from light or usage of thinner substrate to speed up the heating and cooling of the substrate. Nevertheless, the centre of the beam, which corresponds to the peak intensity, is clearly resolvable.

4 Conclusions

We have demonstrated a significant advancement in uncooled photodetection technology through the development of high-performance phototransistors based on sparse SWCNT networks on pyroelectric $LiNbO_3$ crystal. Our innovative approach combines the intrinsic advantages of SWCNTs – tunable bandgap and exceptional carrier mobility —with the pyroelectric properties of $LiNbO_3$ to create devices that operate at room temperature across an unprecedented spectral range. We show that the crucial factor to obtain this output lies in the precisely controlled synthesis of SWCNT networks by means of a modified aerosol CVD method, achieving optimal percolation characteristics that maximize the sensitivity of the network to the gate voltage modulation. This method, coupled with our novel capillary transfer technique, enables the fabrication of uniform, high-quality channels while preserving the intrinsic properties of the nanotubes – length and non-defectiveness. Placed on the polar faces of *z*-cut $LiNbO_3$ pyroelectric crystal, SWCNT sparse network exhibit remarkable sensitivity to the temperature changes induced by direct temperature control as well as visible-infrared light, with specific detectivities improved in comparison to graphene-based alternatives and reaching 1.7×10^{10} cm$\sqrt{\text{Hz}}$/W at 1550 nm and 1.4×10^{10} cm$\sqrt{\text{Hz}}$/W at 9.3 μm for certain phototransistors. We have established clear structure-property relationships governing device performance. Our systematic investigation reveals that low-resistive devices achieve superior absolute responsivities (up to 80 mA/W at 1550 nm), while high-resistive channels excel in relative response (reaching nearly 100 %/μW), providing crucial design principles for application-specific optimization. The consistent ~2-second response time across configurations, which corresponds to the thermal properties of $LiNbO_3$, demonstrates the robust nature of the pyroelectric gating mechanism. Thus, the further development of the devices should be focused on the optimisation of the thermal coupling of the system to improve the speed of the response. In addition, the development of the channel's coating could be worked through to stabilise the reproducibility of the performance and shrink the hysteresis of transfer characteristics. The demonstrated integration of SWCNT network with pyroelectric-based platforms results in a device with a combination of room-temperature operation, broadband response, and exceptional sensitivity, which opens new possibilities for applications ranging from thermal imaging to optical communications. Moreover, our findings suggest that further performance enhancements may be achieved through strategic materials engineering and device architecture optimization, potentially revolutionizing the field of uncooled photodetection, approaching miniaturisation challenging for conventional analogues.

References

1. Rogalski A. *Infrared and Terahertz Detectors* 3rd ed (CRC Press, Boca Raton, 2019). http://doi.org/10.1201/b21951.
2. Vincent JD, Hodges SE, Vampola J et al. *Fundamentals of Infrared and Visible Detector Operation and Testing* (Wiley, New York, 2015). http://doi.org/10.1002/9781119011897.
3. Hossain A, Rashid MH. Pyroelectric detectors and their applications. *IEEE Trans Ind Appl* **27**, 824–829 (1991).
4. Hsieh CY, Chen YT, Tan WJ et al. Graphene-lead zirconate titanate optothermal field effect transistors. *Appl Phys Lett* **100**, 113507 (2012).
5. Fang HJ, Lin ZY, Wang XS et al. Infrared light gated MoS_2 field effect transistor. *Opt Express* **23**, 31908 (2015).
6. Gopalan KK, Janner D, Nanot S et al. Mid-infrared pyroresistive graphene detector on $LiNbO_3$. *Adv Opt Mater* **5**, 1600723 (2017).
7. Sassi U, Parret R, Nanot S et al. Graphene-based mid-infrared room-temperature pyroelectric bolometers with ultrahigh temperature coefficient of resistance. *Nat Commun* **8**, 14311 (2017).
8. Shimatani M, Ogawa S, Fukushima S et al. Enhanced photogating via pyroelectric effect induced by insulator layer for high-responsivity long-wavelength infrared graphene-based photodetectors operating at room temperature. *Appl Phys Express* **12**, 025001 (2019).
9. Wei L, Qian JJ, Dong L et al. Wavelength-selective, narrowband graphene transistor with a plasmon-enhanced pyroelectric gate. *Adv Photonics Res* **4**, 2300009 (2023).
10. Liu YF, Chen HW, Zhang YW et al. Highly sensitive MoS_2 photodetector on polarized thin-film lithium niobate with extremely low dark current. *Mod Phys Lett B* **39**, 2450459 (2025).
11. Lv L, Zhuge FW, Xie FJ et al. Reconfigurable two-dimensional optoelectronic devices enabled by local ferroelectric polarization. *Nat Commun* **10**, 3331 (2019).
12. Guan HY, Hong JY, Wang XL et al. Broadband, High-sensitivity graphene photodetector based on ferroelectric polarization of lithium niobate. *Adv Opt Mater* **9**, 2100245 (2021).
13. He ZG, Guan HY, Liang XJ et al. Broadband, polarization-sensitive, and self-powered high-performance photodetection of hetero-integrated MoS_2 on lithium niobate. *Research* **6**, 0199 (2023).
14. Zheng R, Yan MY, Li C et al. Pyroelectric effect mediated infrared photoresponse in Bi_2Te_3/$Pb(Mg_{1/3}Nb_{2/3})O_3$-$PbTiO_3$ optothermal ferroelectric field-effect transistors. *Nanoscale* **13**, 20657–20662 (2021).
15. Weis RS, Gaylord TK. Lithium niobate: summary of physical properties and crystal structure. *Appl Phys A* **37**, 191–203 (1985).
16. Volk T, Wöhlecke M. *Lithium Niobate* (Springer, Berlin, Heidelberg, 2009). http://doi.org/10.1007/978-3-540-70766-0.
17. Womg KK. *Properties of Lithium Niobate* (The Institution of Engineering and Technology, London, 2002).
18. Radamson HH. Graphene. In Kasap S, Capper P. *Springer Handbook of Electronic and Photonic Materials* (Springer, Cham, 2017). http://doi.org/10.1007/978-3-319-48933-9_48.
19. Léonard F. *The Physics of Carbon Nanotube Devices* (William Andrew, Norwich, 2009).
20. Burdanova MG, Tsapenko AP, Kharlamova MV et al. A review of the terahertz conductivity and photoconductivity of carbon nanotubes and heteronanotubes. *Adv Opt Mater* **9**, 2101042 (2021).
21. He XW, Léonard F, Kono J. Uncooled carbon nanotube photodetectors. *Adv Opt Mater* **3**, 989–1011 (2015).
22. Jiang QY, Wang KK, Wang F et al. High-performance photodetectors based on suspended ultralong carbon nanotubes. *ACS Nano* **18**, 25249–25256 (2024).
23. Wu WF, Ma H, Cai X et al. High-speed carbon nanotube photodetectors for 2μm communications. *ACS Nano* **17**, 15155–15164 (2023).
24. An PP, Kovalyuk VV, Gladush YG et al. High-speed optical-waveguide integrated single-walled carbon nanotube bolometer. *Appl Phys Lett* **125**, 201101 (2024).
25. Komrakova S, An P, Kovalyuk V et al. Hybrid silicon nitride photonic integrated circuits covered by single-walled carbon nanotube films. *Nanomaterials* **13**, 2307 (2023).
26. Yamashita S. Nonlinear optics in carbon nanotube, graphene, and related 2D materials. *APL Photonics* **4**, 034301 (2019).
27. Novikov IV, Krasnikov DV, Lee IH et al. Aerosol CVD carbon nanotube thin films: from synthesis to advanced applications: a comprehensive review. *Adv Mater* **37**, 2413777 (2025).
28. Marcus MS, Simmons JM, Castellini OM et al. Photogating carbon nanotube transistors. *J Appl Phys* **100**, 084306 (2006).
29. Sczygelski E, Sangwan VK, Wu CC et al. Extrinsic and intrinsic photoresponse in monodisperse carbon nanotube thin film transistors. *Appl Phys Lett* **102**, 083104 (2013).
30. Alena AA, Krasnikov DV, Livshits GB et al. Films enriched with semiconducting single-walled carbon nanotubes by aerosol N_2O etching. *Carbon* **212**, 118094 (2023).
31. Serebrennikova SI, Kopylova DS, Gladush YG et al. Photogating interfacial effects in carbon nanotube-based transistors on a Si/SiO_2 substrate toward highly sensitive photodetection. *Nanoscale* **15**, 19351–19358 (2023).
32. Alekseeva A, Livshits GB, Klimovich AS et al. Temporary tattoo transfer of sub-percolating single-walled carbon nanotube films for high-yield thin film transistor arrays (2025). https://www.ssrn.com/abstract=5082496.
33. Itkis ME, Borondics F, Yu AP et al. Bolometric infrared photoresponse of suspended single-walled carbon nanotube films. *Science* **312**, 413–416 (2006).
34. Kopylova DS, Boldyrev NY, Iakovlev VY et al. A bolometer based on single-walled carbon nanotubes and hybrid materials. *Quantum Electron* **46**, 1163–1169 (2016).
35. Kopylova DS, Fedorov FS, Alekseeva AA et al. Holey single-walled carbon nanotubes for ultra-fast broadband bolometers. *Nanoscale* **10**, 18665–18671 (2018).
36. Kurtukova TN, Kopylova DS, Raginov NI et al. Plasma-treated carbon nanotubes for fast infrared bolometers. *Appl Phys Lett* **122**, 093501 (2023).
37. Moisala A, Nasibulin AG, Brown DP et al. Single-walled carbon nanotube synthesis using ferrocene and iron pentacarbonyl in a laminar flow reactor. *Chem Eng Sci* **61**, 4393–4402 (2006).
38. Khabushev EM, Krasnikov DV, Zaremba OT et al. Machine learning for tailoring optoelectronic properties of single-walled carbon nanotube films. *J Phys Chem Lett* **10**, 6962–6966 (2019).
39. Khabushev EM, Krasnikov DV, Kolodiazhnaia JV et al. Structure-dependent performance of single-walled carbon nanotube films in transparent and conductive applications. *Carbon* **161**, 712–717 (2020).
40. Repelin Y, Husson E, Bennani F et al. Raman spectroscopy of lithium niobate and lithium tantalate. Force field calculations. *J Phys Chem Solids* **60**, 819–825 (1999).
41. Kocabas C, Pimparkar N, Yesilyurt O et al. Experimental and theoretical studies of transport through large scale, partially aligned arrays of single-walled carbon nanotubes in thin film type transistors. *Nano Lett* **7**, 1195–1202 (2007).
42. Zavodchikova MY, Kulmala T, Nasibulin AG et al. Carbon nanotube thin film transistors based on aerosol methods. *Nanotechnology* **20**, 085201 (2009).
43. Kim W, Javey A, Vermesh O et al. Hysteresis caused by water molecules in carbon nanotube field-effect transistors. *Nano Lett* **3**, 193–198 (2003).
44. Sun YL, Xie D, Dai RX et al. Ferroelectric polarization effect on hysteresis behaviors of single-walled carbon nanotube network field-

effect transistors with lead zirconate-titanate gating. *Curr Appl Phys* **18**, 324–328 (2018).
45. Duong DL, Lee SM, Lee YH. Origin of unipolarity in carbon nanotube field effect transistors. *J Mater Chem* **22**, 1994–1997 (2012).
46. Imaeda H, Ishii S, Kishimoto S et al. Observation of n-type conduction in carbon nanotube field-effect transistors with Au contacts in vacuum. *Jpn J Appl Phys* **51**, 02BN06 (2012).
47. Fang HH, Hu WD. Photogating in low dimensional photodetectors. *Adv Sci* **4**, 1700323 (2017).

Acknowledgements

Y.G.G. and A.G.N. are thankful for the RSF grant (number 22-13-00436-П, SWCNT synthesis and characterization).

Author contributions

Conceptualization: SIS, DSK, YGG, SM, AGN. Methodology: DSK, YGG, SM, SSZ, DVK. Investigation: SIS, DSK, YGG, SM, NEG, ARV, AVA, SSZ. Data curation: SIS, DSK, YGG, SM. Validation: SIS, DSK, YGG, SM, ARV, AVA, SSZ, DVK. Visualization: SIS, NEG. Supervision: YGG, SM, AGN. Resources: YGG, SM, DVK. Funding acquisition: YGG, AGN. Writing—original draft: SIS, DSK, YGG, SM. Writing—review & editing: SIS, DSK, YGG, SM, NEG, ARV, AVA, SSZ, DVK, AGN.

Competing interests

The authors declare that they have no competing interests.

Supplementary information

Supplementary information for this paper is available at
https://doi.org/10.29026/oea.2026.260019